Stochastic Eutectic Growth

K. R. Elder,[1] François Drolet,[1] J. M. Kosterlitz,[2] and Martin Grant[1]
[1]*Department of Physics, McGill University, Rutherford Building, 3600 University Street, Montréal, Québec, Canada H3A 2T8*
[2]*Department of Physics, Brown University, Providence, Rhode Island 02912*
(Received 1 July 1993)

A full phase field model of eutectic growth is proposed, which incorporates the generic features of a eutectic phase diagram and reduces to the sharp-interface model in the appropriate limit. Large scale two-dimensional simulations are presented for the isothermal solidification of a uniformly undercooled eutectic melt, in which the Avrami exponent is 3. The results of this study identify three possible growth mechanisms: diffusion limited growth, lamellar growth, and spinodal decomposition.

PACS numbers: 64.70.Dv, 05.70.Fh, 82.20.Mj

A eutectic is characterized by a point in the temperature concentration plane (T, C) known as the eutectic point at which a liquid coexists with two solid phases of different concentration. Isothermal solidification of a eutectic liquid is a complex process involving the nucleation and growth of two solid phases and can lead to a multitude of microstructures. The study of the kinetics of such pattern formation and domain growth has been greatly enhanced by the concepts of universal dynamical scaling. It is now generally accepted [1,2] that systems with conserved and nonconserved order parameters form separate universality classes defined in part by power law growth of the average domain size with dynamical exponents x of $1/3$ and $1/2$, respectively. Eutectic solidification involves the coupling of conserved concentration and nonconserved liquid/solid order parameter fields. To investigate this, a full phase field model is introduced. A phase field model is needed for this study since the standard sharp-interface model [3–6], used for directional eutectic growth in which a liquid/solid interface is pulled through a temperature gradient, cannot treat the stochastic nature of nucleation and is difficult to implement for a collection of multivalued interfaces. To verify the model and corresponding discrete map, many known results for directional eutectic solidification [3,5] are recovered. Finally large scale numerical simulations of isothermal eutectic solidification from an undercooled melt are presented. These indicate three possible growth mechanisms for the concentration field: diffusion limited growth ($x = 1/2$), lamellar growth ($x = 0$), and spinodal decomposition or Ostwald ripening ($x = 1/3$).

The model is presented in terms of a free energy $\mathcal{F}$ which is a functional of $c \propto C - C_E$, the deviation from the eutectic concentration, and a liquid/solid order parameter ψ. To lowest order, $\mathcal{F}$ can be written as

$$\mathcal{F}\{c,\psi\}=\int d\mathbf{r}[f(c,\psi)+K_\psi|\nabla\psi|^2/2+K_c|\nabla c|^2/2], \quad (1)$$

where $f(c,\psi) = -r\psi^2/2 + u\psi^4/4 + (\alpha\Delta T - \beta c^2)\psi + wc^2/2 + bc^4/4$, $\Delta T = T - T_m$ with T_m the melting temperature at $\beta = 0$, and the other parameters are phenomenological constants. Solid (liquid) phases are represented by $\psi > 0$ ($\psi < 0$). T is fixed externally, which is an excellent approximation for 2D films, metals, and metalloids where concentration diffusion is orders of magnitude slower than that of T, so latent heat generated by the transition may be ignored. The dynamics is realized by Langevin equations,

$$\partial\psi/\partial t = -\Gamma_\psi(\delta\mathcal{F}/\delta\psi) + \eta_\psi, \quad (2)$$

$$\partial c/\partial t = \Gamma_c\nabla^2(\delta\mathcal{F}/\delta c) + \eta_c. \quad (3)$$

$\Gamma_{c,\psi}$ are mobilities, $\langle\eta_\psi(\mathbf{r},t)\eta_\psi(0,0)\rangle = 2\Gamma_\psi k_b T\delta(\mathbf{r})\delta(t)$, and $\langle\eta_c(\mathbf{r},t)\eta_c(0,0)\rangle = 2\Gamma_c k_b T\nabla^2\delta(\mathbf{r})\delta(t)$. The mean-field phase diagram of this model is illustrated in Fig. 1 for parameters $(r,b,w,\alpha,\beta) = (1,1,0,0.15,0.15)$. Also included in this diagram are the metastable extensions of the liquidus and solidus lines. When $w < \beta(r/u)^{1/2}$ and $\alpha(r/u)^{1/2} \ll 1$, the eutectic point is given by

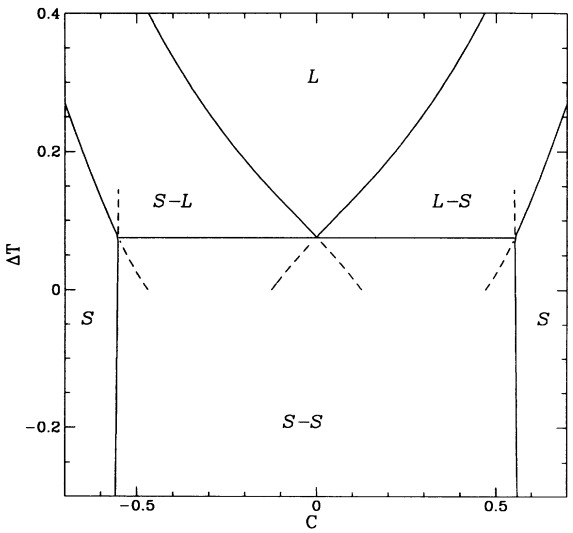

FIG. 1. Phase diagram of Eq. (1) for $(r,b,w,\alpha,\beta)=(1,1,0,0.15,0.15)$. Dashed (solid) lines: boundaries of metastable (stable) phases. $\mathcal{S}$ ($\mathcal{L}$) is solid $\psi > 0$ (liquid $\psi < 0$) phase.

$(\Delta T_E, c_E) \approx ([2\beta(r/u)^{1/2} - w]^2/8b\alpha, 0)$. Similar expressions can be derived for the coexistence lines and chemical potential μ. Phase field modeling of liquid/solid transitions has been described elsewhere [7].

The sharp-interface model can be obtained from Eqs. (2) and (3) using standard techniques [8,9] in the appropriate limit. The two assumptions that must be made are that the interface of width ξ is in local thermodynamic equilibrium and that the curvature is small or $\kappa\xi \gtrsim 0$. Also, the interface must exist. Note that the phase field model provides a phenomenological description of eutectic growth even when growth cannot be described by an interface model. The Gibbs-Thomson condition is $\delta c/c_{\rm mis} = \pm[d_0\kappa + (\Delta T - \Delta T_E)/mc_{\rm mis}]$, where $d_0 = \sigma/(c_{\rm mis}^2 \partial\mu/\partial c)$, $\sigma = 2K_c \int du(\partial c^p/\partial u)^2$, $c_{\rm mis}$ is the miscibility gap, m is the slope of the liquidus, c^p is a stationary planar interface at $\Delta T = \Delta T_E$, and δc and ΔT are evaluated at the interface. The plus and minus signs refer to the $c < 0$ and $c > 0$ phases. Integration of Eq. (3) across a moving interface gives $v_n(c_s - c_l)\hat{\mathbf{n}}\cdot\hat{\mathbf{y}} = D_l \partial\delta c/\partial u|_l - D_s \partial\delta c/\partial u|_s$, where the subscripts l and s refer to the liquid and solid sides of the interface and v_n is the velocity normal to the interface. The diffusion constants are given by $D_{l,s} = \Gamma_c(\partial^2 f/\partial c^2)|_{l,s}$. These boundary conditions and the fact that Eq. (3) reduces to a diffusion equation in the liquid and solid phases comprise the sharp-interface model [3–6].

For computational efficiency, a simple discrete map was constructed from Eqs. (2) and (3) using Euler's method for the time derivative and a nearest neighbor approximation for the Laplacians. This was simulated on both square and hexagonal lattices with time step 0.05, mesh size 1.3, $\Gamma_\psi = \Gamma_c = r = b = K_c = 1$, and $\beta = \alpha$. As a consequence of the universality of domain growth, the continuum model, discrete map, and sharp-interface model are all equally valid phenomenological models of eutectic growth, which has been exploited in many numerical studies [2]. To support this, the map was used to recover many known results [3,5] on directional eutectic growth.

Directional eutectic growth is implemented numerically through $\Delta T = G(y - vt)$, where y is the pulling direction and v is the pulling velocity. In these simulations, $(G, \alpha, w, K_\psi) = (0.01, 0.15, 0.01, 1)$. For a given v, steady state interface profiles were obtained as a function of lamellar wavelength λ and, as in other works [3,5], the minimum undercooling assumption was used to select λ and the average interfacial undercooling $\Delta\bar{T}_m$. Details will be reported in a future paper. A summary of this study is shown in Fig. 2 in which the following well-known [3,5,10] relationships were obtained: $\lambda^{-2} \propto v$ [Fig. 2(a)] and $(\Delta\bar{T}_m - \Delta T_E)^2 \propto v$ [Fig. 2(b)]. Discrete branches of solutions exist for different initial conditions [5]. The recently discovered [4,5,11,12] tilt wave instability was studied by fixing λ and increasing v until the lamellae undergo a tilting transition. Figure 2(c) shows the tilt

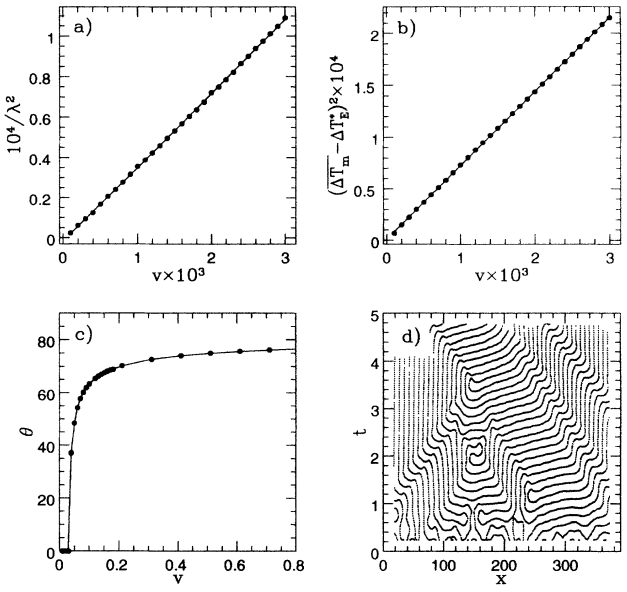

FIG. 2. Simulation of directional eutectic growth. v as function of (a) $1/\lambda^2$; (b) $(\Delta\bar{T}_m - \Delta T_E^*)^2$; (c) tilt angle ($\theta$). (d) Points are solid/solid interface position ten lattice spaces behind the liquid/solid front as a function of time.

angle θ as a function of v, where $\theta = 0°$ corresponds to lamellae that are perpendicular to the interface. All these results are consistent with earlier simulations [5]. Tilt waves can also be generated by random initial conditions at sufficiently large v [Fig. 2(d)] or by thermal fluctuations.

Using the same discrete map, a 2D numerical study of isothermal solidification of a uniformly undercooled eutectic liquid was performed on a hexagonal lattice with periodic boundary conditions and $c_0 = c_E = 0$. Nucleation and growth of solid droplets and the phase separation process are illustrated respectively in the first and second columns of Fig. 3. The parameters used are $(K_\psi, w, \alpha, \Delta T) = (1/8, 0, 0.15, -0.4)$ on a system of size 256×256 with thermal fluctuations of magnitude 0.29 in ψ. The initial undercooled liquid state is represented as $\psi(x, y) = -1 + \eta$ and $c(x, y) = \eta$, where $|\eta| \leq 0.1$ is random. The third column of Fig. 3 corresponds to a second type of simulation in which a small solid droplet is incorporated in the initial conditions but without thermal fluctuations. The system size was 512×512 and the parameters were $(K_\psi, w, \alpha, \Delta T) = (1, 0, 0.15, -0.2)$. In these and other simulations, the lamellar wavelength λ^* selected decreased with increasing interface velocity v which is proportional to ΔT, although the minimum undercooling assumption cannot be made as ΔT is fixed.

The statistics of ordering for the first set of simulations was analyzed by monitoring the solid volume fraction $X(t)$ and the spherically averaged structure factors of both fields: $S_\psi(k, t) \equiv \langle|\psi(\mathbf{k}, t)|^2\rangle$ and $S_c(k, t) \equiv$

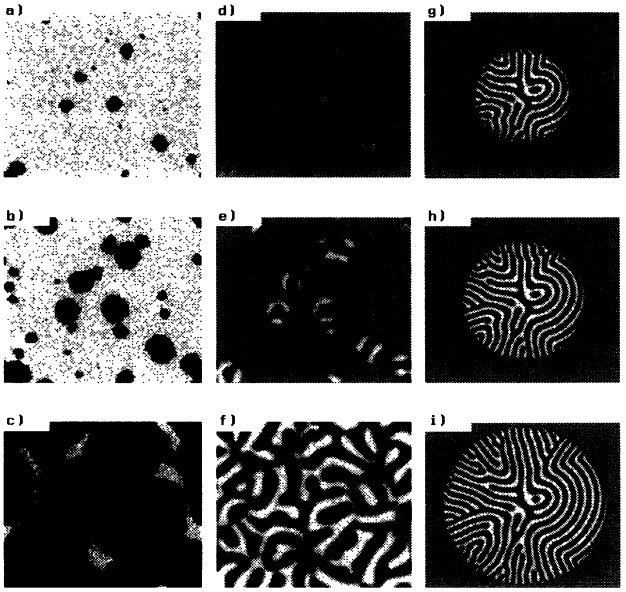

FIG. 3. Grey scale plots of ordering fields. In (a) to (c) black, solid ($\psi > 0$); light grey, liquid ($\psi < 0$) at times $t = 1000$, 1600, and 3150. (d) to (f) are counterparts of (a) to (c) for concentration field. White: $c = -0.6$; black: $c = 0.6$. (g) to (i) show concentration field at $t = 2500$, 3750, and 5000. See text for parameters and initial configurations.

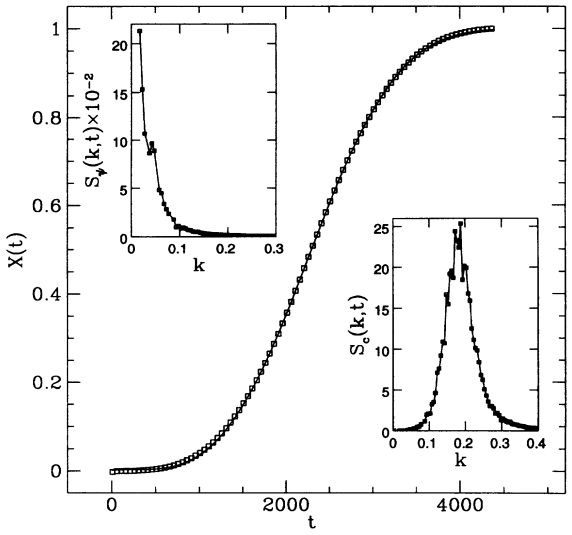

FIG. 4. Open squares: solid volume fraction $X(t)$; the solid line is a fit to the Kolmogorov [13] form given in the text. Top left inset: Sample structure factor for ψ field at $t = 2500$. Bottom right inset: Sample structure factor for c field also at $t = 2500$.

$\langle|c(\mathbf{k},t)|^2\rangle$. The results were averaged over 33 independent runs. $X(t)$ can be fitted by a Kolmogorov [13] form with an Avrami exponent of 3: $X(t) = 1 - e^{-\frac{\pi}{3}Iv^2(t-t_0)^3}$, where I is the nucleation rate and t_0 the waiting time. The fit and sample structure factors for both fields are shown in Fig. 4. $S_\psi(k,t)$ shows poor quantitative agreement with Sekimoto's expression [14].

The peak position k_m, height $S_m \equiv S_c(k_m,t)/\langle c^2\rangle$, and width w of $S_c(k,t)$ are displayed in Fig. 5. Before interpreting these results, it is useful to consider several simple examples. At late times, when $X(t) = 1$, Eq. (3) reduces to the Cahn-Hilliard-Cook [15] model of spinodal decomposition. In this limit, k_m/w and $S_m k_m^d$ are constant and $k_m \propto t^{-x}$ with $x = 1/3$. $2\pi/k_m$ is interpreted as the average domain size. In contrast, if the domain size λ^* is fixed, then k_m is also and S_m is proportional to the average size of the growing droplets. Since domains grow at constant v and $S_m \propto 1/w$, $1/w \propto t^1$. This is seen in the last column of Fig. 3 and will be termed lamellar growth. If a collection of uncorrelated solid droplets each consisting of a set of stripes or lamellae in c of average size $2\pi/k_m$ is considered, the structure factor takes the form $S_c(k,t)/\langle c^2\rangle \approx k_m^{-d}(k_m/w)f([k-k_m]/w)$. In principle w and k_m are both time-dependent quantities.

During the early stages of growth, both $(S_m w/k_m)^{1/2}$ and $1/k_m$ increase as $t^{1/2}$. In this time regime, the initial lamellar wavelength is smaller than λ^* and is increasing at the expense of the surrounding liquid matrix. This diffusion limited process leads to an exponent of 1/2. As the droplets coalesce, spinodal decomposition takes over, which will eventually give an exponent of 1/3. The smaller exponent seen in Fig. 5 ($x \approx 1/4$) is simply a precursor to the asymptotic exponent of 1/3. Many numerical studies [2] have shown that the dynamic exponent in spinodal decomposition starts at a value smaller

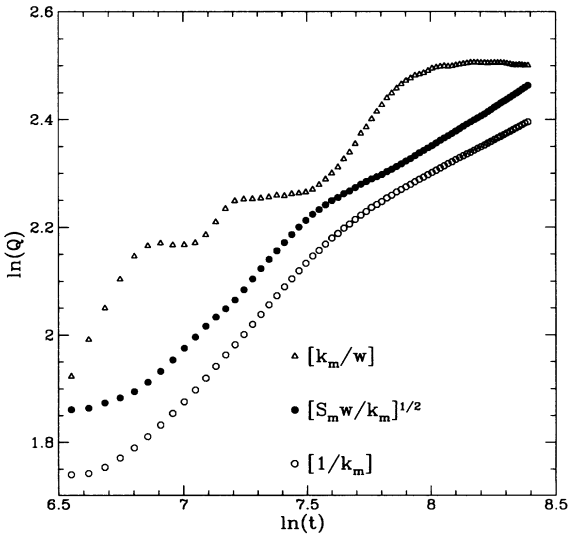

FIG. 5. Open circles, solid circles, and open triangles correspond to $\ln(Q) = \ln(1/k_m) + 0.55$, $\ln([S_m w/k_m]^{1/2}) + 1.7$, and $\ln(k_m/w)$, respectively.

than 1/3. These simulations may also be hampered by an initial state that contains lamellar structures.

The dynamics of k_m/w provides additional insight into the ordering. Most striking are the three distinct plateaus seen in Fig. 5. Figures 3(d) and 3(e) indicate that the first and second plateaus correspond to the growth of the initial drop of precipitate and the next shell or layer of the opposite phase, respectively. The width w decreases as the second shell grows since it is highly correlated with the initial precipitate. The last plateau corresponds to spinodal decomposition occurring when the sample is approximately 90% solidified.

To summarize, three distinct growth mechanisms have been identified. Initially, diffusion limited growth occurs as shown in Figs. 3(d) and 3(e) leading to a growth exponent of 1/2. If the solid drops are allowed to grow large without coalescence, as in Figs. 3(g) to 3(i), lamellar ordering occurs in which $k_m \propto t^0$ and $w \propto t^{-1}$. Finally when the solid drops coalesce spinodal decomposition takes over as in Fig. 3(f). For this model, spinodal decomposition, or Ostwald ripening for off-eutectic concentrations, will be the infinite time mechanism. However, which growth mechanisms can be observed depends on the quench.

Preliminary experimental results on the eutectic crystalization of amorphous metallic glasses have been reported by Fischer *et al.* [16]. In these experiments, both the small and large angle time resolved x-ray scattering patterns are measured, which respectively measure correlations in the electron density (c) and the crystal structure (ψ). Thus the scaling exponents should be directly measurable. However, direct comparisons are complicated by differences in the average density of the amorphous and crystal phases and lattice mismatches at grain boundaries. We are presently incorporating some of these features to better describe such experiments.

This work is supported by the Natural Sciences and Engineering Research Council of Canada and le Fonds pour la Formation des Chercheurs et l'Aide à la Recherche de la Province de Québec. J.M.K. was partially supported by NSF Grant No. DMR-9222812. We thank Dr. Mark Sutton, Dr. Henry Fisher, Dr. Ian Graham, and Dr. Mohamed Laradji for useful discussions.

[1] J. D. Gunton, M. San Miguel, and P. S. Sahni, in *Phase Transitions and Critical Phenomena*, edited by C. Domb and J. L. Lebowitz (Academic, London, 1983), Vol. 8.

[2] Y. Oono and S. Puri, Phys. Rev. Lett. **58**, 836 (1987); S. Puri and Y. Oono, Phys. Rev. A **38**, 1542 (1988); T. M. Rogers, K. R. Elder, and R. C. Desai, Phys. Rev. B **37**, 9638 (1988).

[3] K. A. Jackson and J. D. Hunt, Trans. Metall. Soc. AIME **236**, 843 (1966); **236**, 1129 (1966).

[4] Alain Karma, Phys. Rev. Lett. **59**, 71 (1987).

[5] K. Kassner and C. Misbah, Phys. Rev. Lett. **65**, 1458 (1990); **66**, 445 (1991); Phys. Rev. A **44**, 6513 (1991); **44**, 6533 (1991).

[6] J. S. Langer, Phys. Rev. Lett. **44**, 1023 (1980); V. Datye and J. S. Langer, Phys. Rev. B **24**, 4155 (1981).

[7] A. A. Wheeler, G. B. McGadden, and W. J. Boettinger, Phys. Rev. E **47**, 1893 (1993); A. A. Wheeler, B. T. Murray, and R. J. Schaefer, Physica (Amsterdam) **66D**, 243 (1993).

[8] B. Grossmann, H. Guo, and M. Grant, Phys. Rev. A **43**, 1727 (1991); J. B. Collins and H. Levine, Phys. Rev. B **31**, 6119 (1985).

[9] K. R. Elder, J. Viñals, and M. Grant, Phys. Rev. Lett. **68**, 3024 (1992); Phys. Rev. A **46**, 7618 (1992).

[10] In Ref. [5] deviations from $\lambda \propto v^{-1/2}$ and $\Delta\bar{T}_m - \Delta T_E^* \propto v^{1/2}$ were observed at small v and explained by corrections to the exponent 1/2. We also see deviations from 1/2 but prefer to explain them by corrections to scaling, $\lambda \propto v^{-1/2} + b$. The data of Ref. [5] are also consistent with this form.

[11] G. Faivre, S. De Cheveigne, C. Guthmann, and P. Kurowski, Europhys. Lett. **9**, 779 (1989).

[12] B. Caroli, C. Caroli, and S. Faivre, J. Phys. I (France) **2**, 281 (1992).

[13] A. N. Kolmogorov, Bull. Acad. Sci. USSR, Phys. Ser. **3**, 335 (1938).

[14] K. Sekimoto, Physica (Amsterdam) **135A**, 328 (1986).

[15] J. W. Cahn and J. E. Hilliard, J. Chem. Phys. **28**, 258 (1958); J. W. Cahn, Acta Metall. **14**, 1685 (1966); Trans. Metall. Soc. AIME **242**, 166 (1968); H. E. Cook, Acta Metall. **18**, 297 (1970).

[16] H. E. Fischer, S. Brauer, J. O. Ström-Olsen, M. Sutton, and G. B. Stephenson, in *Interface Dynamics and Growth*, edited by K.S. Liang, Materials Research Society Symposium Proceedings No. 237 (MRS, Pittsburgh, 1992).

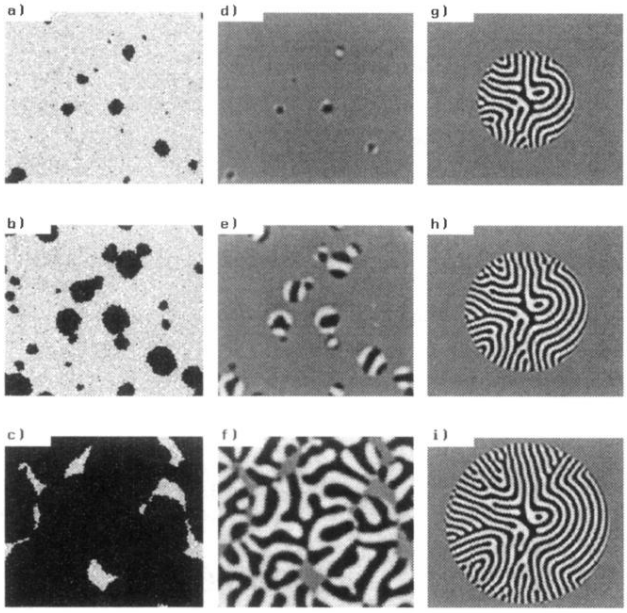

FIG. 3. Grey scale plots of ordering fields. In (a) to (c) black, solid ($\psi > 0$); light grey, liquid ($\psi < 0$) at times $t = 1000$, 1600, and 3150. (d) to (f) are counterparts of (a) to (c) for concentration field. White: $c = -0.6$; black: $c = 0.6$. (g) to (i) show concentration field at $t = 2500$, 3750, and 5000. See text for parameters and initial configurations.